AIAA Aviation
22-26 June 2015, Dallas, TX
21st AIAA/CEAS Aeroacoustics Conference

# Harmonic and Broadband Separation of Noise from a Small Ducted Fan

Alexander Truong* and Dimitri Papamoschou†
*University of California, Irvine, Irvine, CA, 92697, USA*

**In the study of noise from propellers and ducted fans, rigorous signal decomposition into harmonic and broadband components is essential for the development of high-fidelity predictive models. Current spectral methods and phase averaging techniques lack the temporal resolution to compensate for fluctuations in operating condition intrinsic to real world experiments. In this paper we use a Vold-Kalman filter to extract the tonal and broadband content of noise from a small ducted fan simulating the conditions of an ultra-high-bypass turbofan engine. The fan operated at pressure ratio of 1.15 and tip Mach number of 0.61. The investigation includes time traces, narrowband spectra, one-third octave spectra, and overall sound pressure level. The energies of the tonal and broadband components are similar at low frequency, while the broadband component dominates at high frequency. In addition, there are distinct differences in the directivities of the two components. The trends are in general agreement with NASA large-scale fan tests at transonic conditions.**



## Nomenclature

| | | |
|---|---|---|
| $A$ | = | structural equation matrix |
| BPF | = | blade passing frequency |
| $C_k$ | = | complex phasor matrix |
| $f(t)$ | = | instantaneous frequency |
| FPR | = | fan pressure ratio |
| $i$ | = | imaginary unit $=\sqrt{-1}$ |
| $I$ | = | identity matrix |
| $J(x)$ | = | cost function |
| $r$ | = | weighting factor |
| SPL | = | sound pressure level |
| $t$ | = | time |
| $x_k(t)$ | = | time-varying (complex) envelope of order $k$ |
| $y(t)$ | = | total measured acoustic signal |
| $\varepsilon(t)$ | = | error in structural equation fit |
| $\eta(t)$ | = | broadband or shaft-uncorrelated noise |
| $\theta$ | = | polar angle relative to downstream axis |
| $\phi$ | = | azimuthal angle |
| $\nabla^p x_k[n]$ | = | structural equation of order p |
| () | = | round brackets denote continuous signals |
| [] | = | square brackets denote discrete signals |

*Subscripts and Superscripts*

| | | |
|---|---|---|
| $H$ | = | Hermitian |
| $k$ | = | harmonic or order of signal |
| $T$ | = | transpose |

*Graduate Student Researcher, Department of Mechanical Aerospace Engineering, Member AIAA
†Professor, Department of Mechanical and Aerospace Engineering, Fellow AIAA

# I. Introduction

It has been over 50 years since the Boeing 707 ushered in both the jet age and the era of federal mandates requiring minimum noise standards for aircraft entering service. These regulations are becoming increasing stringent, motivating considerable research effort to suppress noise and understand the physical processes of sound generation. For instance, the aviation community has set ambitious targets for the development of ultra-quiet commercial aircraft, encapsulated by NASA's N+2 and N+3 noise goals. Candidate propulsion schemes revolve around the high-bypass turbofan and the open rotor. Attainment of the noise goals requires not only improvements at the component level, but also a systems integration approach for the design of the propulsor and the airframe. The shielding of engine noise by the airframe has been of particular interest, with recent efforts addressing fan inlet[1] , jet[2,3] , and open-rotor noise.[4,5] The blended wing body (BWB) airplane concept has been central to these efforts because its layout is amenable to innovative integration concepts and its aerodynamic efficiency is superior to that of conventional airplane designs.[6]

Effective shielding of the fan noise requires knowledge of the source characteristics. This impacts the entire aircraft design because decisions such as the placement of the engines, geometry of the elevon, and positioning of the vertical fins are driven not only by aerodynamics but also acoustic considerations. Noise assessment requires the determination of the tonal and broadband components to properly assess the efficacy of migration strategies and for validating prediction codes. Fan harmonic components are integer multiples of the fundamental frequency (the so-called orders), i.e., engine rotational speed. On the other hand, broadband noise is random in nature and is generated from an array of source mechanisms such as turbulence interaction noise, rotor-stator interaction noise, and trailing edge noise.[7] Each noise component, tonal or broadband, can have different directivity.

The NASA Glenn Research Center (GRC), has conducted numerous large scale experimental investigations, such as the fan source diagnostic test (SDT).[8–15] These experiments are obviously very expensive. The small scale paradigm enables significant cost and time savings in the acoustic evaluation of noise-reduction concepts. Sterolithographic fabrication enables the three-dimensional "printing" of the complex geometry of fan blades and the nacelle structure that are nearly impossible to fabricate using conventional machining. The rapid-prototyping approach has been used successfully with jet noise testing of realistic nozzle configurations and open-rotor spinning at full-scale tip speed powered by high-performance DC motors.[2,5] More recently, assessments of the relevance of UCI's small scale ducted fan indicate that small-scale models reproduce with good fidelity the main acoustic features[16] .

Knowledge of the tonal and broadband noise content is essential for predicting and optimizing propulsion-airframe integration. Even when tones strongly protrude from the background, the decomposition of the tonal and broadband noise components establishes the importance of broadband noise.[17] Tonal isolation techniques include peak-finding algorithm, moving medium curve, phase averaging, and Sree's Method.[4,17–19] However, frequency domain methods cannot easily localize information in the time domain, nor compensate for fluctuations intrinsic to real world experiments. A recent NASA SDT investigation employed a Vold-Kalman signal processing technique to filter out the harmonic noise sources.[20,21] This tool performs a time-domain decomposition of a measured signal into phase-accurate time history of fan harmonic and broadband constituents. The output from the filter has a much higher resolution and dynamic range than a Fast Fourier Transform (FFT) or phase averaging procedure. In a similar fashion, this study applies the Vold-Kalman order tracking to acoustics measurements of a small duct fan.

The goals of this study were to: (1) extract the tonal and broadband components from a small-scale simulator that captures the physics of fan noise generation using a Vold-Kalman filter; and (2) investigate the spectral and directivity characteristics of the tonal and broadband noise sources.

# II. Experimental Details

## A. Ducted Fan Rig

The ducted fan rig and its operation have been described in a previous publication;[16] here we review the salient elements relevant to the present study. The scale of the fan is approximately 1:38, based on a full-scale inlet diameter of 2.67 m (105 in.). The fan was designed to simulate the low fan pressure ratio (high bypass ratio) operation of a geared turbofan engine. Various design elements of the rotor and stators were extracted from published reports based on NASA/GE Source Diagnostic Test (SDT), particularly Refs. 9, 11, and 12. The specifications are summarized in Table 1, and the design is illustrated in Fig. 1. A

bell-mouth entry for the nacelle was chosen to prevent flow separation in the static test environment. The nacelle (including the stators) and rotor were manufactured from plastic material using stereolithograpy. The nacelle features pressure ports for measuring the inlet static pressure and the outlet total pressure. The aerodynamic performance was assessed by these pressure measurements.

**Table 1. Ducted fan specifications**

| | Parameter | Specifications |
|---|---|---|
| **Nacelle** | Fan inlet diameter | 70.0 mm |
| | Fan exit diameter | 71.0 mm |
| | Nacelle exit to inlet area ratio | 0.56 |
| | Design fan pressure ratio | 1.15 |
| | Input power | 5.0 kW (6.7 hp) |
| **Rotor** | Overall design | Based on GE R4 fan |
| | Count | 14 |
| | Diameter | 69.2 mm (0.4 mm tip clearance) |
| | Design RPM | 57000 |
| | Design Tip Mach | 0.61 |
| | Hub-to-Tip ratio | 0.42 |
| | Solidity | 1.34 at pitch line |
| | Blade Airfoil | NACA 65-series |
| | Blade Camber | 56.6 ° (hub) to 6.2 ° (tip) |
| | Blade Pitch Angle | 51.6 ° (hub) to 28.3 ° (tip) |
| | Blade Thickness/Chord Ratio | 0.081 (hub) to 0.028 (tip) |
| **Stator** | Overall design | Radial vane, based on low-count SDT configuration |
| | Count | 24 |
| | Solidity | 2.21 (hub) to 1.04 (tip) |
| | Blade Airfoil | NACA 65-Series |
| | Blade Camber | 42.2 ° (hub) to 40.6 ° (tip) |
| | Blade Thickness/Chord Ratio | 0.0707 (hub) to 0.0698 (tip) |

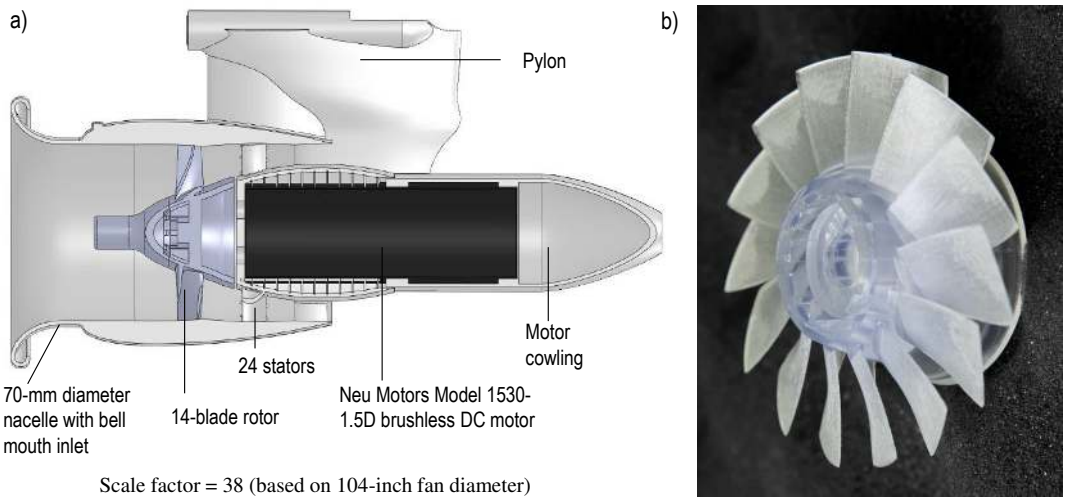


**Figure 1. Overview of the ducted fan design. a) Cross-sectional view; b) picture of the 3D printed rotor.**

The rotor was powered by a high-performance brushless DC motor (Neu Motors, Model 1530-1.5D) which can attain a surge power of 5.0 kW. The motor has an RPM/Volt (Kv) rating of 1350, meaning that it can spin at an RPM of 60,000 at the maximum rated voltage of 44 V. The motor was controlled using Castle Creations Phoenix 160 Amp electronic speed controller (ESC). Power to the speed controller was supplied by two 6S (22.2 $V$) lithium-ion polymer (Lipo) battery connected in series with a discharge rate of 30c and a capacity of 8300 mAh. The speed controller was controlled by a Spektrum AR6200 DSM2 six-channel receiver connected wirelessly to a Spektrum DX7 2.4 GHz seven-channel radio. The receiver was powered by a Castle Creations battery eliminator circuit (BEC PRO). The power components and their installation are depicted in Fig. 2.

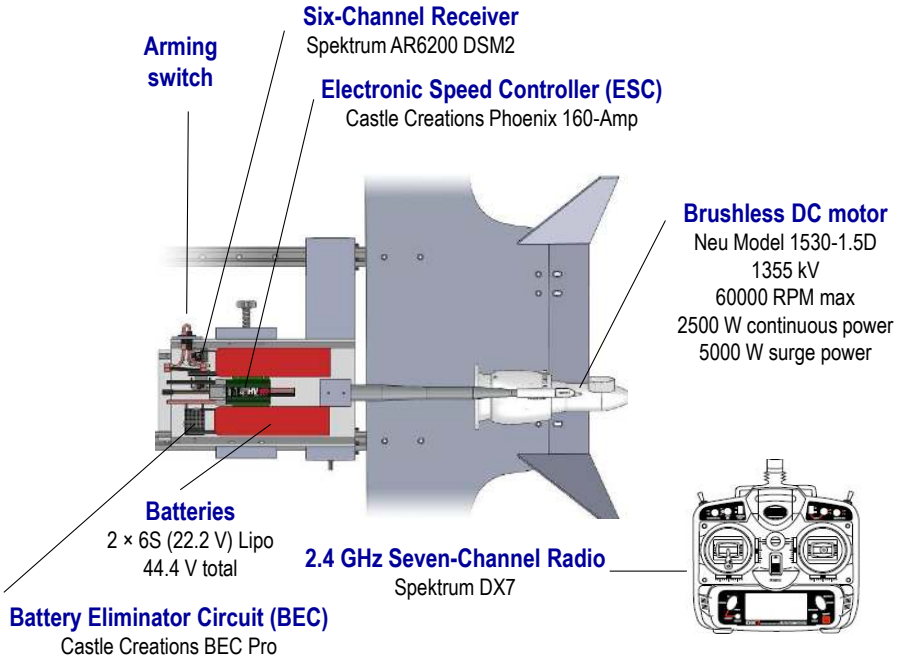


**Figure 2. Principal power components and their installation.**

## B. Test Facility

Acoustic measurements were conducted inside an anechoic chamber at UC Irvine's Aeroacoustics Facility, depicted in Figs. 3 and 4. Twenty-three 3.2-mm condenser microphones (Brüel & Kjaer, Model 4138) with a frequency response of 140 kHz were used to survey the far-field acoustics. The microphones were arranged twelve on a downward arm (azimuth angle $\phi = 0°$) and eleven on a sideline arm ($\phi = 60°$). The polar angle $\theta$ is defined from the center of the fan exit plane relative to the downstream rotor axis, as shown in Fig. 3. Its approximate range was 15° to 110° for the downward arm, and 15° to 100° for the sideline arm. The minimum microphone-to-nacelle distance was 0.8 m, or 11.4 fan diameters. This places the microphones in the acoustic far field for the frequency range relevant to aircraft noise (i.e., higher than 50 Hz at full scale).

The microphones were connected, in groups of four, to six conditioning amplifiers (Brüel & Kjaer, Model 2690-A-0S4). The 23 outputs of the amplifiers were sampled simultaneously, at 250 kHz per channel, by three eight-channel multi-function data acquisition boards (National Instruments PCI-6143). A 24th output channel was assigned to the RPM sensor. National Instruments LabView software was used to acquire the signals. The temperature and humidity inside the anechoic chamber were recorded to enable computation of the atmospheric absorption.

The sampling rate for each microphone was 250000 samples/second, and the number of samples for each test run was 262144 per microphone. The signals were re-sampled at constant angular increments of the shaft for computing the order tracking.[22] The narrowband sound pressure level spectra were computed with a 8192-point Fast Fourier Transform, giving a frequency resolution of 30.5 Hz. The SPL narrowband

spectra were corrected for actuator response, free-field correction, and atmospheric absorption, resulting into lossless spectra. The full-scale, 1/3-octave spectrum was calculated from the lossless narrowband spectrum after dividing the frequency vector by the scale factor of 38. In addition, the overall sound pressure level (OASPL) was calculated from the lossless SPL spectrum. The lab-scale SPL narrowband spectrum, lab-scale OASPL, and full-scale 1/3-octave spectrum, are referenced to a distance of 305 mm (12 in.) from the exit of the ducted fan. Time series analysis did not include frequency-based corrections.

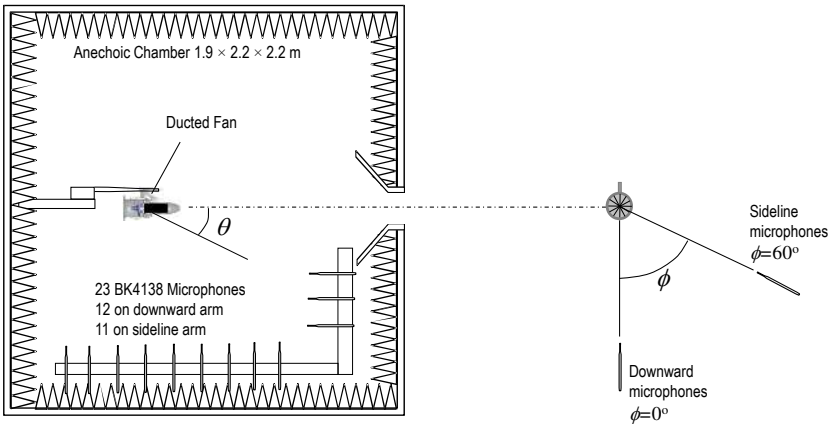


**Figure 3. Aeroacoustic test setup and geometry conventions.**

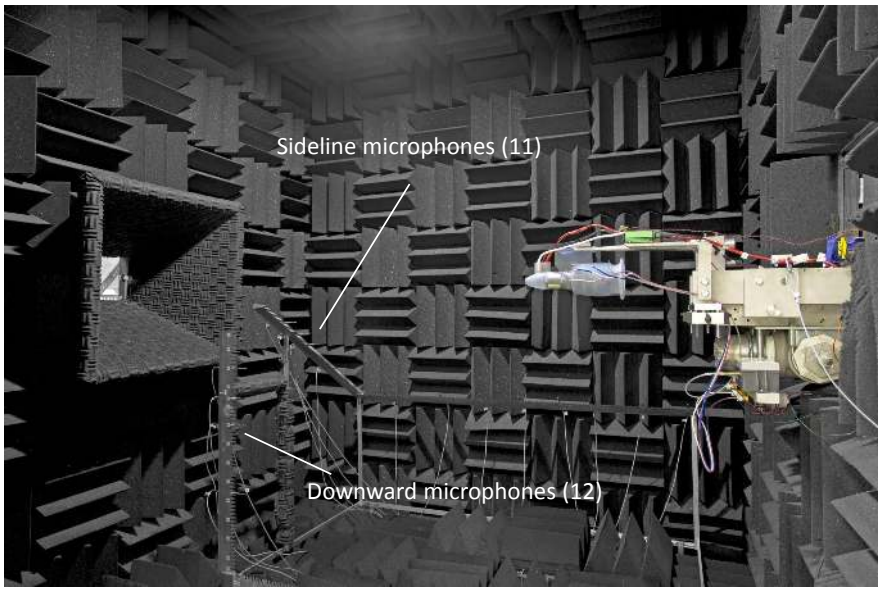


**Figure 4. Picture of ducted fan tested inside anechonic chamber.**

Instantaneous rotor speed was determined by detection of the pulsation of the electrical load from the electronic speed controller (ESC) to the motor, using a ferrite toroid Hall effect sensor as shown in Fig. 5. The ESC sends a pulse-width modulated (PWM) waveform to the motor. The pulses are emitted at the commutation frequency, $f_c$ , which is the rate of switching of the polarity of the magnets to maintain the motor rotation. The pulse width controls the power to the motor. The raw signal voltage from the Hall effect sensor is reduced to levels tolerated by the data acquisition system using a voltage divider circuit, and is then fed to a low-pass filter and through a buffer. The low-pass filter attenuates the fast switching PWM component of the signal, while the buffer prevents unacceptable loading of the voltage divider circuit by the low-pass filter circuit. Once digitized, a more aggressive high order low-pass Chebyshev filter is applied to cutoff frequency higher than the commutation frequency. The period of the signal is then computed using the time lag between the peaks as shown in the middle image in Fig. 5. Conversion from the commutation

period $T$ to instantaneous frequency (BPF) is given by the formula $f(t) = 2N_b/(TN_p)$, where $N_p$ is the number of magnetic poles in the motor and $N_b$ is the number of blades. The Neu 1530 motor has four poles, and the rotor has 14 blades. This method enabled the determination of a precise phase accurate frequency for each acoustic test run (the RPM signal was collected simultaneously with the microphone signals).

A representative time history of the motor frequency is plotted in Fig. 6. The low-pass filtered signal of the instantaneous frequency is depicted by the red line. It is observed that the shaft frequency fluctuates at a high frequency over a slowly varying RPM value that slows during the experiment. A key to the successful implementation of the Vold-Kalman filter is the precise knowledge of the structure to be tracked. The non-filtered (black) signal serves as a very accurate RPM input to the Vold-Kalman filter, such that the tracking filter will follow the peaks of the tones (orders) instead of tracking the wrong frequency.

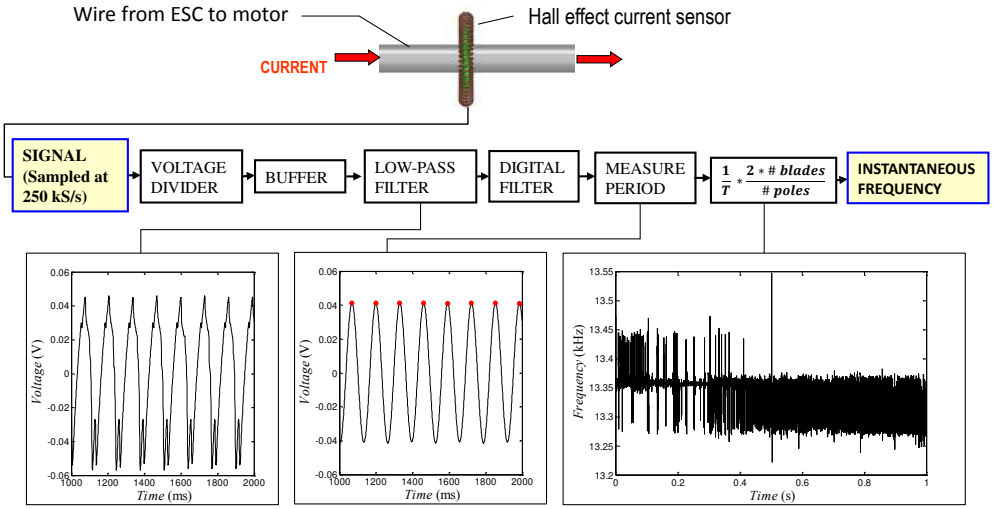


**Figure 5. Flowchart of RPM measurement and phasor frequency determination process.**

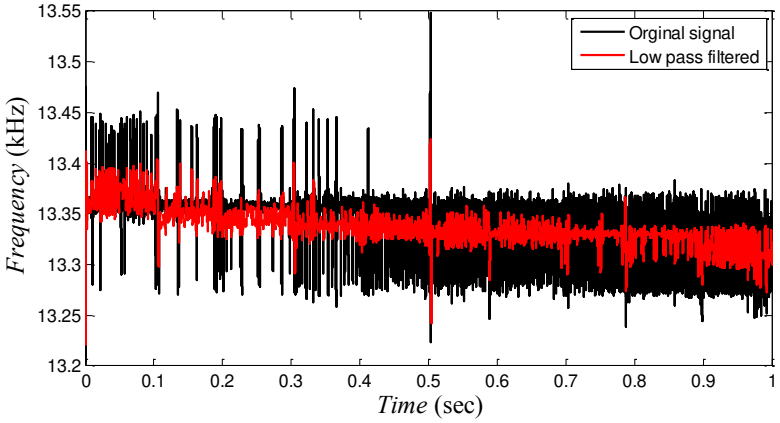


**Figure 6. Frequency time trace during a typical test run (262144 samples). The red line represents the low-pass filtered component of the RPM sensor output. Rotor speed indicates an average RPM near 57,000 (13.33 kHz). The rotor slows down slightly during the experiment.**

## III. Algorithum of the Vold-Kalman Filter

The Vold-Kalman filter, introduced by Vold and Leuridan,[23] extracts the non-stationary periodic components from a signal using a known frequency vector (e.g., rotor RPM). Several additional works describe its functionality and applications.[21,24,25] The filter is formulated as a least-squares problem and can be solved as a linear system. Similar to the Kalman filter, which is based on the process/ measurement equations (i.e. state-space model) and a global estimator (orthogonal projection)[26] , the Vold-Kalman filter is based on the

structural/data equations and a global estimator (least squares). Only the second-generation multi-order Vold-Kalman filter will be reviewed and applied in this paper.

### A. Data Equation

Engineers are interested in signals that exhibit periodicity, i.e., events that occur repeatedly in time with a prescribed period.[27] This may be a result of an oscillating spring/membrane, mechanical systems, or the sound pressure generated by the periodic volume displacement of air by the blades of a propeller. These are deterministic processes. Broadband noise, in contrast, is typically generated by a more or less stochastic process. Such noise sources include turbulence, vortex shedding, interaction effects, and represent everything that is uncorrelated with the RPM sensor signal. An arbitrary real-valued signal can be modeled as a summation of a deterministic periodic part consisting of $K$ sine waves with varying phase and amplitude, plus a stochastic part of uncorrelated broadband noise $\eta(t)$. This sinusoidal plus noise formulation is called the Wold decomposition.[28] The total measured signal $y(t)$ is of the form:

$$y(t) = \sum_{k=1}^{K} x_k(t) \exp\left(2\pi k i \int_0^t f(t)dt\right) + \eta(t) \tag{1}$$

Here the deterministic periodic signal is written in complex polar coordinates, with $k$ indicating the order extracted. The exponential term is called the complex phasor and represents a constant-amplitude, frequency-modulated carrier wave. The instantaneous frequency $f(t)$ of the carrier wave is determined by the tachometer or RPM sensor. The slowly time-varying (complex) amplitude $x_k(t)$ modulates the carrier wave (i.e. the complex phasor). The objective of the Vold-Kalman algorithm is to minimize the sum of squares of the errors (e.g., broadband signal) for a number of harmonics by properly choosing the complex envelope $x_k(t)$. Storing the complex phasor on the diagonals of the matrix $C_k$, the above expression takes the compact form:

$$y(t) - \sum_{k=1}^{K} C_k x_k(t) = \eta(t) \tag{2}$$

### B. Structural Equation

The structural equation imposes smoothness on the complex envelope $x_k(t)$ by means of a backward finite-difference sequence. This is accomplished by minimizing the error $\varepsilon(t)$ made in the smoothness of the envelope, where the smoothness is represented by a low-order polynomial. The polynomial order designates the number of the filter poles. The equations for 1-,2-, and 3- pole filter coefficients are found by the Pascal triangle:

$$\nabla x_k[n] = x_k[n] - x_k[n-1] = \varepsilon_k[n] \tag{3a}$$

$$\nabla^2 x_k[n] = x_k[n] - 2x_k[n-1] + x_k[n-2] = \varepsilon_k[n] \tag{3b}$$

$$\nabla^3 x_k[n] = x_k[n] - 3x_k[n-1] + 3x_k[n-2] - x_k[n-3] = \varepsilon_k[n] \tag{3c}$$

Assuming a second-order difference, the system of structural equations with the complex envelope $x_k$ for order $k$ as the unknown takes the form of a matrix equation:

$$\begin{bmatrix} 1 & -2 & 1 & 0 & \cdots & & & \\ 0 & 1 & -2 & 1 & 0 & \cdots & & \\ \vdots & 0 & 1 & -2 & 1 & 0 & \cdots & \\ & \vdots & 0 & \ddots & \ddots & \ddots & 0 & \cdots \\ & & & & 1 & -2 & 1 & 0 \\ 0 & 0 & 0 & 0 & & 1 & -2 & 1 \end{bmatrix} \begin{bmatrix} x_k[1] \\ x_k[2] \\ x_k[3] \\ \vdots \\ \\ \\ \\ x_k[n] \end{bmatrix} = \begin{bmatrix} \varepsilon_k[3] \\ \varepsilon_k[4] \\ \varepsilon_k[5] \\ \vdots \\ \\ \\ \\ \varepsilon_k[n] \end{bmatrix} \tag{4}$$

Notice that the errors $\varepsilon_k[1]$ and $\varepsilon_k[2]$ cannot be determined since the stencil contains points outside the domain of the complex envelope. For an order $k$, the matrix on the left hand side is a sparse band matrix

(tridiagonal matrix in this example) with dimensions of $(N-p)\times N$, $p$ being the number of the filter poles ($p=2$ in this example). In compact notation the matrix reads as:

$$Ax_k = \varepsilon_k \tag{5}$$

### C. The Least-Squares Problem

The set of data and structural equations creates an over-determined linear system for the desired waveform amplitude $x_k(t)$. No exact solution exists, nor does a two-sided inverse. A pseudo inverse can be obtained using ordinary least-squares, QR decomposition, or the singular value decomposition (SVD). Normally, the Vold-Kalman filter uses least squares because of speed. Here, the objective is to estimate the non-random complex envelope $x_k(t)$ by minimizing the square of the errors from the data and structural equations due to non-periodic components and envelope roughness, respectively. Introducing a scalar weighing factor $r$, a cost function is formulated to find the optimum solution in the sense of least squares:

$$J(x) = \sum_{k=1}^{K} r_k^2 \varepsilon_k^H \varepsilon_k + \eta^H \eta \tag{6}$$

The purpose of the weighting factor is to slant the prominence of the structural equation with that of the data equation. For instance, if $r$ is large the cost function is strongly influenced by the structural equation yielding a very smooth modulator. The value of $r$ also determines the bandwidth of the filter. Large $r$ results in very small bandwidth and vice-versa. The minimum is found by evaluating the derivative $dJ/dx^H = 0$, and rearranging to a more familiar "normal" least-squares form:

$$\left(r^2 A^T A + I\right) x_k = C_k^H y \tag{7}$$

The equivalent "second-derivative" minimization requirement for a multidimensional problem is that the symmetric hessian matrix $(r^2 A^T A + I)$ be positive definite. It can be shown that $r^2 A^T A + I$ is positive semi-definite, and adding the identity matrix turns it positive definite. This property ensures that the matrix on the left hand side is invertible. Moreover, the matrix $r^2 A^T A + I$ is independent of the tracked frequency in $C_k$ and the signal $y$. This allows for the matrix to be reused for tracking of orders with different phasors, reducing the extensive computational memory resource required. With regards to rotor noise separation, no crossing orders exist. Efficient Vold-Kalman filtering is accomplished using multi-order tracking through a single order scheme by simply changing the terms in the phasor term on the right hand side of Eq. 7 for different harmonics, and solving the respective linear system independently. For instance, given the high sampling rate necessitated by small scale acoustical experiments, and the multiple orders tracked, the single order scheme drastically shrinks the matrix dimension from 1,750,000 to solving 7 decoupled matrices with dimension of 250,000. The expanded version of Eq. 7 for a two-pole Vold-Kalman filter and order $k$ has the form:

$$\begin{bmatrix} r+1 & -2r & r & 0 & \cdots & & \\ -2r & 5r+1 & -4r & r & 0 & \cdots & \\ \vdots & r & -4r & 6r+1 & -4r & 0 & \cdots \\ 0 & 0 & 0 & \ddots & \ddots & \ddots & \ddots \end{bmatrix} \begin{bmatrix} x_k[1] \\ x_k[2] \\ x_k[3] \\ \vdots \\ \\ x_k[n] \end{bmatrix} = \begin{bmatrix} C_k^H y[1] \\ C_k^H y[2] \\ C_k^H y[3] \\ \vdots \\ \\ C_k^H y[n] \end{bmatrix} \tag{8}$$

The linear system is very large, sparse, banded, and positive definite. This implies that the solution can be obtained efficiently by using Cholesky factorization. In the process of determining a solution the matrix on the right hand side undergoes zero-phase low-pass filtering. The frequency response characteristic, defined by a -3 dB drop in magnitude, is controlled by the value of the weighting coefficient $r$. Fig. 7 depicts the bandwidth of the filter with varying pole counts and a weighting factor. A higher weighting factor results in a smaller bandwidth and a smoother varying amplitude as shown in the figure. However, the value of $r$ should not overshadow the effect of adding unity to the main diagonal. Typical Vold-Kalman order tracking codes utilize a two-pole filter.

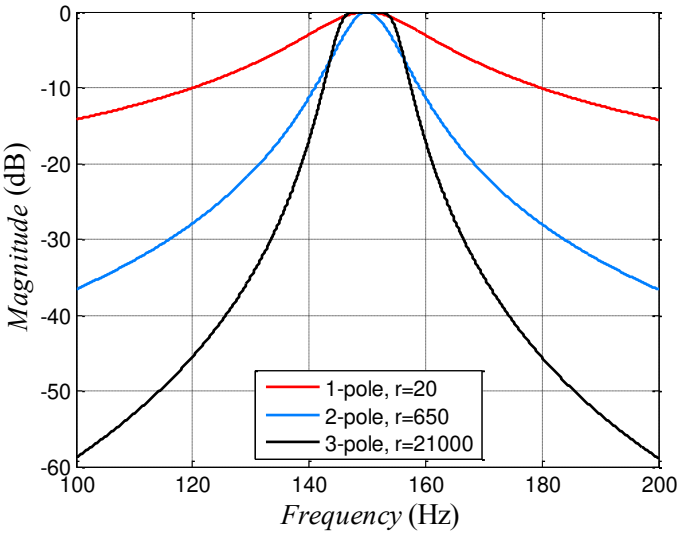


**Figure 7. Vold Kalman filter transfer function for various pole counts.**



### D. Comparison With Other Transforms

There are some similarities between the Vold-Kalman filter and other non-stationary time-frequency methods such as wavelets, chirplets, Hilbert transform, and Hilbert Huang transform.[29] Here we discuss commonalities with the Hilbert transform since wavelets are a subset of the Hilbert transform. The main advantage of the finite impulse response filter-Hilbert method over wavelet convolution is that the filter-Hilbert method allows more control over the frequency characteristic of the filter, whereas the filter shape of a Morlet wavelet or chirplet is always Gaussian.[30] On the other hand, the Hilbert-Huang transform is a way to decompose a complex signal into its basis time series (intrinsic mode function), to which the Hilbert transform can be applied.[31]

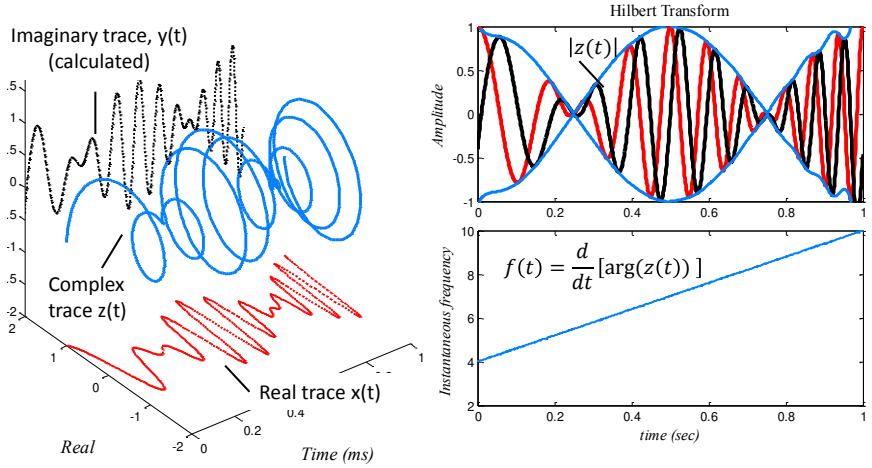


**Figure 8. The Hilbert transform in complex space-time. The analytic signal in complex space is projected onto the real axis to form the signal. Projection onto the imaginary axis (quadrature) shifts the phase of the real signal by 90°. This complex signal can be written as a complex phasor with amplitude and phase: $a(t)e^{i2\pi ft}$.**

A complex sinusoidal signal is defined by its amplitude and phase. It can be represented using Euler's formula: $a(t)e^{i2\pi ft}$. Here $a(t)$ is the time varying amplitude and the exponential represents the oscillation. This notation can be explained as a vector (phasor) at the origin of the complex plane having a length $a(t)$ and angular position $2\pi ft$. This representation is useful for narrow-band signals, where $a(t)$ is usually "slow" compared to the signal temporal variations. The signal can be represented in a three-dimensional space as depicted in Fig. 8. In this complex space-time the real value signal $x(t)$ measured by a transducer is confined to the real plane, and $y(t)$ is the Hilbert transform of $x(t)$ and is confined to the imaginary

axis. When $x(t)$ and $y(t)$ are added vectorially, the result is a complex analytic trace $z(t) = x(t) + iy(t)$, in the shape of a helical spiral extending along the time axis.[32] Analytic means that the complex signal satisfies the Cauchy-Riemann conditions, that is, the derivative of $z(t)$ is path-independent and unique. The reason for converting the real signal into a complex trace is because the instantaneous amplitude and frequency can be calculated by taking the magnitude and argument of $z(t)$, as shown in the right image of Fig. 8. The real-valued signal of the Vold-Kalman filter is analogous to the filtered real-valued signal $x(t)$ in the Hilbert transform.[21] However, the phase of the signal is computed from the tachometer signal rather than computing the mapping on the imaginary plane. Since a phase-accurate estimate of the instantaneous frequency is obtained directly from the tachometer, the complex phasor is already known. No unwrapping of the phase (revolute) and application of a Savitzky-Golay filter, or conjugate multiplication of adjacent complex samples ($\arg\{z[n]z^*[n+1]\}$) are required to compute the instantaneous frequency.[32] Thus, the Vold-Kalman filter only requires the linear estimation of the complex envelope $C_k$ (analogous to $|z(t)|$) which is generated by the structural equation rather than the signal itself as in the Hilbert transform. Just like in wavelets, the Vold-Kalman filter is a subset of the more general Hilbert transform were information about the signal phase is obtained a priori.



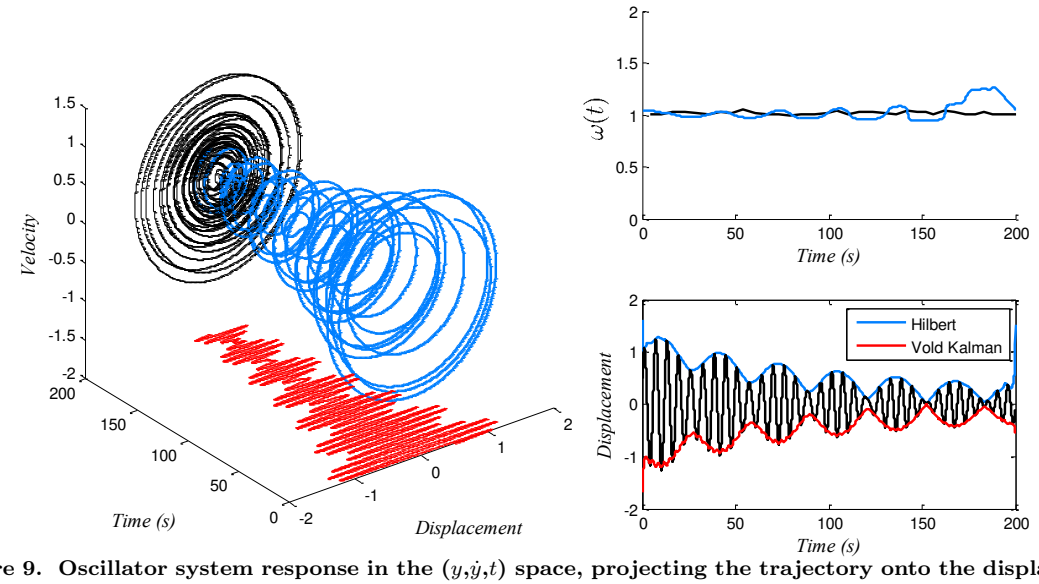


**Figure 9. Oscillator system response in the ($y$,$\dot{y}$,$t$) space, projecting the trajectory onto the displacement time axis gives the measured signal. Mapping the curve to space and velocity gives the phase portrait.**

In Fig. 9, a representative solution for a forced linear oscillator described by the second-order nonautonomous differential equation $\ddot{y}+2\zeta\dot{y}+y = f\cos(\omega t)$ is graphed. $y, t, \zeta, f$, and $\omega$ are the displacement, time, damping ratio, excitation amplitude, and excitation frequency, respectively. Projecting the trajectory onto the displacement time axis gives the measured signal. Mapping the curve to space and velocity gives the phase portrait. White noise was added to the simulated solution. The stationary system is driven near the resonance frequency producing beats. Two times scales are present, an exponentially decaying envelope, and the oscillation corresponding to the natural frequency of the system. The exponential decay is represented by the trajectory inward spiral toward the origin. The linearity of the system implies a constant instantaneous frequency, as illustrated in the right image of Fig. 9. The oscillations are periodic, deterministic, and are modeled by a composition of a small number of monocomponent signals:

$$y(t) = \sum_{k=1}^{K} x_k(t) \exp\left(2\pi k i \int_0^t f(t)dt\right) \tag{9}$$

Non-correlated signals are manifested in the broadband noise term, $\eta(t)$. Here only one order exists, allowing effortless calculation of the complex envelope for both methods; if not, the results of the Hilbert transform are difficult to interpret when the data contain a range of frequencies and filtering or decomposition of the raw signal is required. To capture similar details to the Hilbert transform the Vold-Kalman bandwidth must be tuned. There are several techniques for the estimation of the narrowband signal frequency bandwidth of the Hilbert transform. Nevertheless, when we examine the average variance of the frequency excursion of

the signal around the mean value, the average spectrum bandwidth is:

$$\sigma_{bw}^2 = \int_0^\infty (\omega - \overline{\omega})^2 S(\omega) d\omega = (\overline{\omega^2} - \overline{\omega}^2) + \overline{\dot{A}^2} \tag{10}$$

where $\omega$, $S(w)$, $A$ are the angular frequency, power spectrum, and amplitude of the signal ($A = |z(t)|$). The overbars represent time averages. The equation was obtained from Parseval's theorem and indicates that the average bandwidth is equal to the mean square value of the rate of the amplitude variation plus the mean square value of the deviation from the baseband frequency.[32,33] Using a frequency vector at the natural frequency, the Vold-Kalman filter gives the envelope in red. Alternatively, the filter-Hilbert transform computed similar results as depicted in blue. As noted earlier for the Hilbert transform, the signal phase was derived from the data rather than a tachometer.

Even though the real signal (red) is the same, the trajectory of the integral curve (Fig. 9) does not necessarily match the analytic trace $z(t)$ (Fig. 8), especially for non-linear systems. The addition of a non-linear cubic term $y^3$ to the simple harmonic oscillator, leading to the Duffing oscillator, dramatically changes the picture. Typically, the phase portrait becomes more distorted, generating sharp peaks and troughs in the time series. Additionally, a Duffing oscillator exhibits time variations in its natural frequency.[32,34] In other words, the increased stiffness for large deflections is accompanied by a faster oscillation. Nevertheless, the filter also applies to the limit cycle response of non-linear systems. When the excitation frequencies change, the responses will still be harmonics of the excitation for non-linear structures. Since mechanical systems normally have transfer characteristics dependent upon frequency, the amplitude and phase of these sine waves will typically also change as the periodic loading change their speed.[27] Table 2 compares the Vold-Kalman filter with other noise separation techniques.



**Table 2. Filter comparison**

| | **Spectral Methods** | **Phase Averaging** | **Hilbert Transform** | **Vold-Kalman** | **Sree's Method** |
|---|---|---|---|---|---|
| **Nonstationary** | No | No | Yes | Yes | Yes |
| **Domain** | Frequency | Time | Time | Time | Frequency |
| **Encoder** | No | Yes | No | Yes | No |
| **Filter shape** | No | No | User set | Adaptive bandpass | No |
| **Phase accurate** | No | No | Yes | Yes | No |
| **Processing speed** | Fastest | Medium | Medium | Slowest | Fast |

## IV. Acoustic Results

For all the conditions covered in this report, the RPM was 57200 ± 1.0 % as exemplified in Fig. 6. This corresponds to a rotor tip Mach number of 0.61 ± 1.0 %. Fan exhaust total pressure was 2.2 psig, which translates to FPR=1.15, rotor induced velocity of 87 m/s, fan exit velocity of 155 m/s, and power output of 4400 W (5.9 hp). The calculated power output is consistent with the motor input power of 5 kW and a conversion efficiency of 88 %.

A two-pole second-generation, multi-order using single order scheme Vold-Kalman filter was used to isolate each harmonic from a narrow frequency band around the tracked tone while preserving accurate phase information. To work out the phasor information in the data equation, the tracked tone was determined by the instantaneous frequency of the rotor specified by the RPM sensor. Although the signal consists of a rapidly changing frequency, the Vold-Kalman filter is able to track even at extreme slew rates. Filtering of the 23 microphone data for 7 orders took a few minutes on an Intel Xenon based desktop computer using the Matlab® backslash matrix solver. No down-sampling was applied. Even though extensive exploration of acoustic assessment and shielding effects were investigated in our previous work,[16] signal processing in this paper involves only the isolated ducted fan. In addition, there was no acoustic distinction in the isolated case among the two azimuthal directions. Thus, the results are presented for only the downward azimuthal direction. The acoustic results will be presented as follows:

(a) Time history, plotted for various polar angles, referenced to 305-mm arc.

(b) Narrowband SPL spectra in laboratory scale, referenced to 305-mm arc.

(c) Overall Sound Pressure level (OASPL) in laboratory scale, referenced to 305-mm arc.

(d) Directivity of selected 1/3-octave band levels (full-scale), referenced to 305-mm arc.

(e) Comparison with NASA large scale test, UCI data referenced to a linear traverse displaced 305 mm from the model centerline.

The standard color representation followed throughout this paper is:

- Total measured acoustic signal - Red
- Broadband (difference between raw and BPF Harmonics) - Blue
- BPF Extracted Harmonics (sum of all individual orders) - Black

### A. Decomposition of Time Traces

We first examine the Vold-Kalman decomposition of microphone signals at various polar angles. The results are plotted in Fig. 10. The amplitudes of the noise components are dependent on the polar emission angle. At a polar angle of $\theta = 69.4°$ the amplitude of the overall pressure fluctuation is largest. At polar angles close to the downstream axis, the amplitude of the broadband noise encompasses the majority of the signal. On the other hand, the magnitude of the tonal noise is greatest at $\theta$=69.4°. To properly assess the relative importance of the broadband noise or harmonics, the energy of each waveform must be integrated over a finite octave band interval as done in Section IV.C.

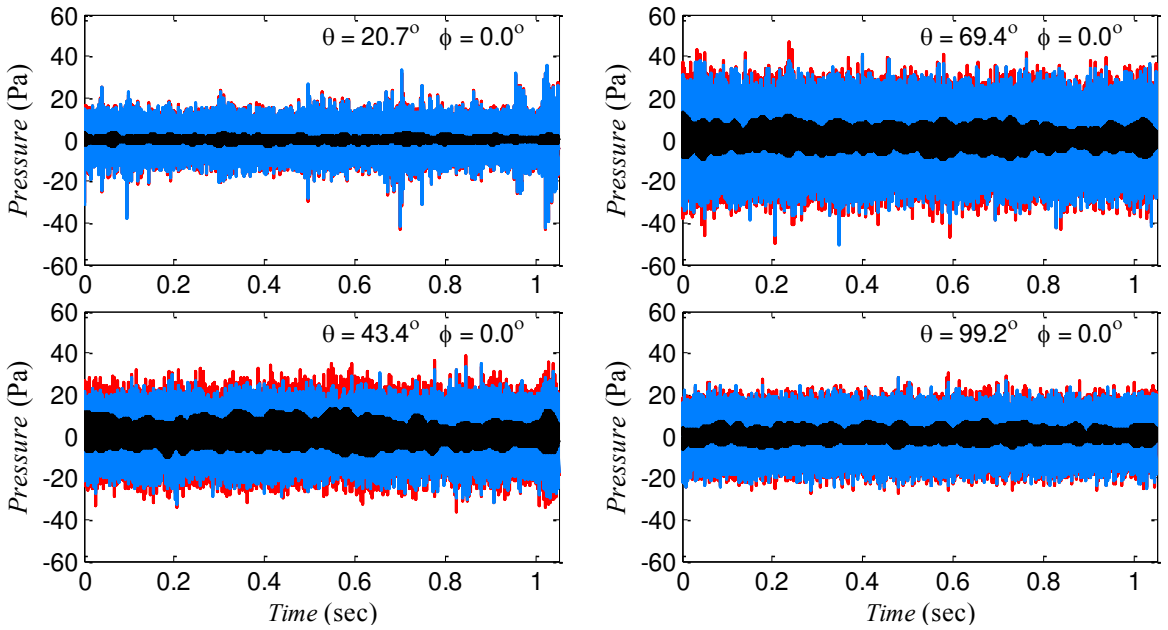


**Figure 10. Time domain signal decomposition of the ducted fan noise at various polar angles. Total signal (red), broadband (blue), harmonic (black).**

### B. Narrowband Spectra

The second set of assessments consists of conventional spectral analysis of the Vold-Kalman filtered signals for two polar angles, $\theta$=20.7° and 99.2°. The SPL narrowband spectra were corrected for actuator response, free-field correction, and atmospheric absorption, resulting into lossless spectra. Narrowband spectra are shown in Fig. 11. Spectral analysis of the microphone signal shows that tones up to 7× BPF were resolved. Hence, seven orders were filtered from the total signal using the Vold-Kalman filter. The Vold-Kalman weighting factor was determined by minimizing the "divots" (or negative peaks) in the broadband spectrum,

giving a bandwidth of 1 Hz. The weighting factor was below the recommended limit described by Tuma for a two-pole, second-generation filter.[24] The black line (middle image) represents the harmonic components that were isolated from the total signal. The bandwidth of each tone relates to the tonal energy removed at that particular order. The sum of the extracted tonal signal forms the BPF harmonic signal. Subtraction of the total signal from the BPF harmonics (black) yields the broadband component (blue). Comparing the spectra at the two polar angles, the harmonic content is more prevalent near the rotational plane ($\theta \sim 90°$).

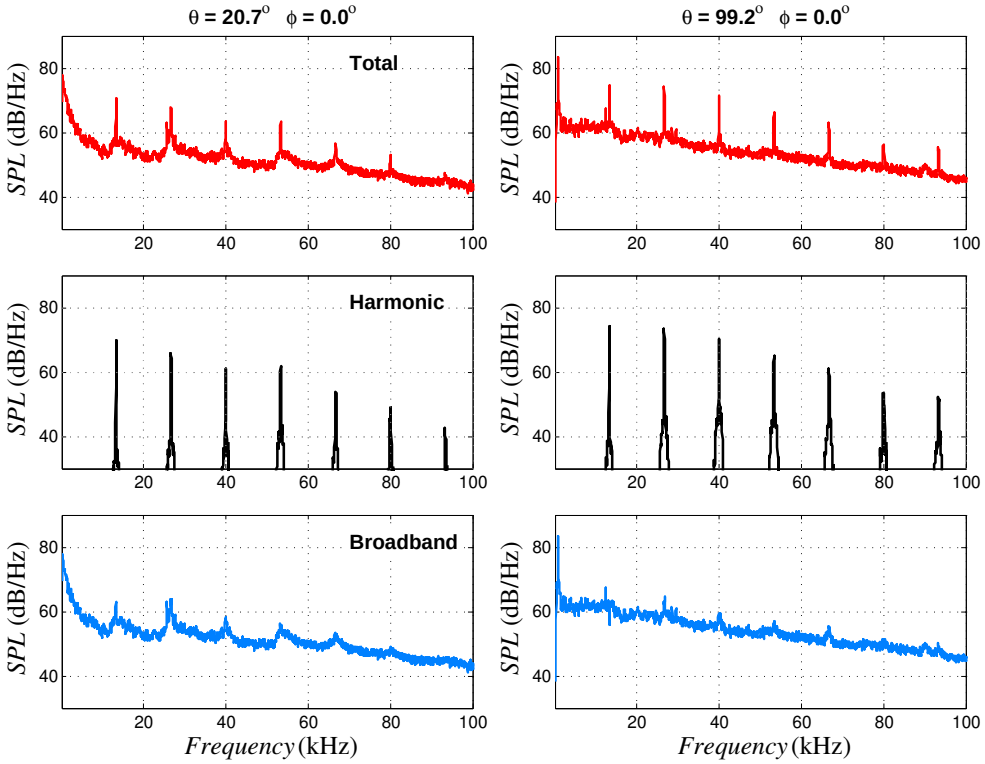


**Figure 11. Narrowband SPL spectra at two polar angles. Total signal (top), harmonic (middle), broadband (bottom).**

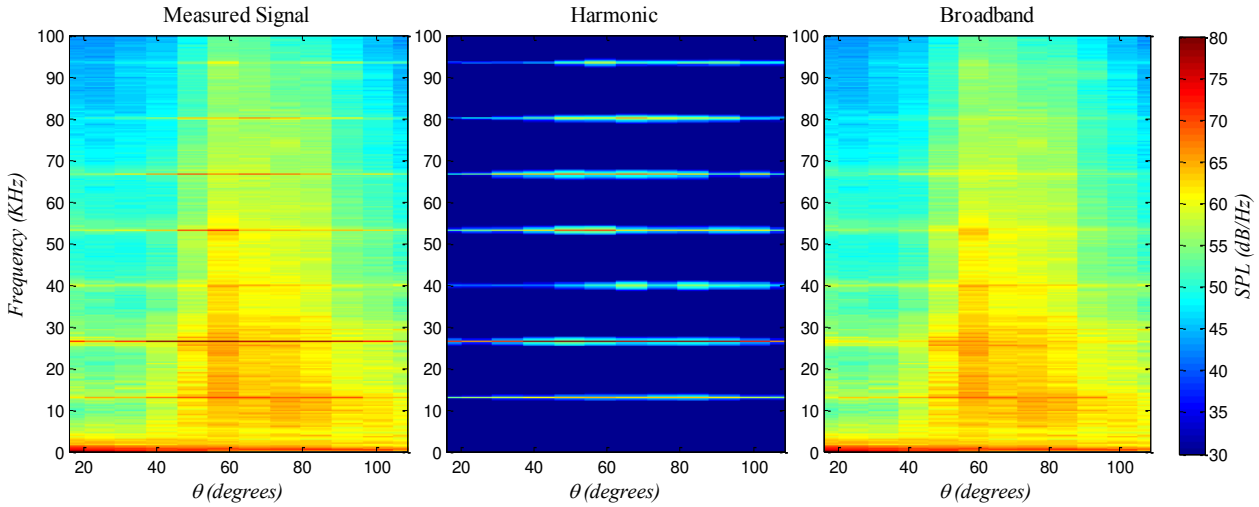


**Figure 12. Countour plots of narrowband SPL spectra.**

Fig. 12 displays contour maps of the SPL versus frequency and polar angle for the total and decomposed signals. As evident in the contour maps of the harmonic component, rotor harmonics ranging from 1×BPF through 7×BPF are extracted. The tonal energy of the filtered (broadband) signal is substantially reduced compared to the measured signal. The broadband signal still retains small remnants of tonal noise, which

is the effect of some broadband noise being weakly correlated with the shaft orders. The subtraction of tonal noise makes a more pronounced impact at low frequency, indicating the relative strength of the tonal component there. Figure 12 also serves to illustrate the directivity of sound versus frequency, with a peak evident near $\theta = 60°$.

### C. Directivity of 1/3-Octave Spectra

Although the narrowband spectra provide a complete representation of the frequency content of the signal, engineering applications often rely on the 1/3-octave spectra. Furthermore, the 1/3 octave spectra allow for the proper assessment of the energy distribution in the harmonic and broadband components.[35] This is essentially a smoothing technique which integrates noise over frequency ranges whose widths are proportional to their center frequencies. The 1/3-octave band spectrum was calculated from the scaled-up, lossless narrowband spectrum by integrating the energy content in each frequency band. We examine the directivity of the following bands, and indicate in parentheses the contained tones: band 9 (1×BPF), band 12 (2×BPF), band 14 (3×BPF), and band 16 (4×BPF and 5×BPF). The directivities of those bands are plotted in Fig. 13. There are significant differences in the direction of peak emission for the various bands, band 9 peaking near $\theta = 80°$ (i.e., close to the plane of rotation), whereas the higher bands peak near $\theta = 50°$. The directivities of the harmonic and broadband components tend to be similar, except for some oscillations in the harmonic content of band 14. It is evident that the energies of the tonal and broadband contents are similar for the lower bands, while the broadband content dominates the higher bands.

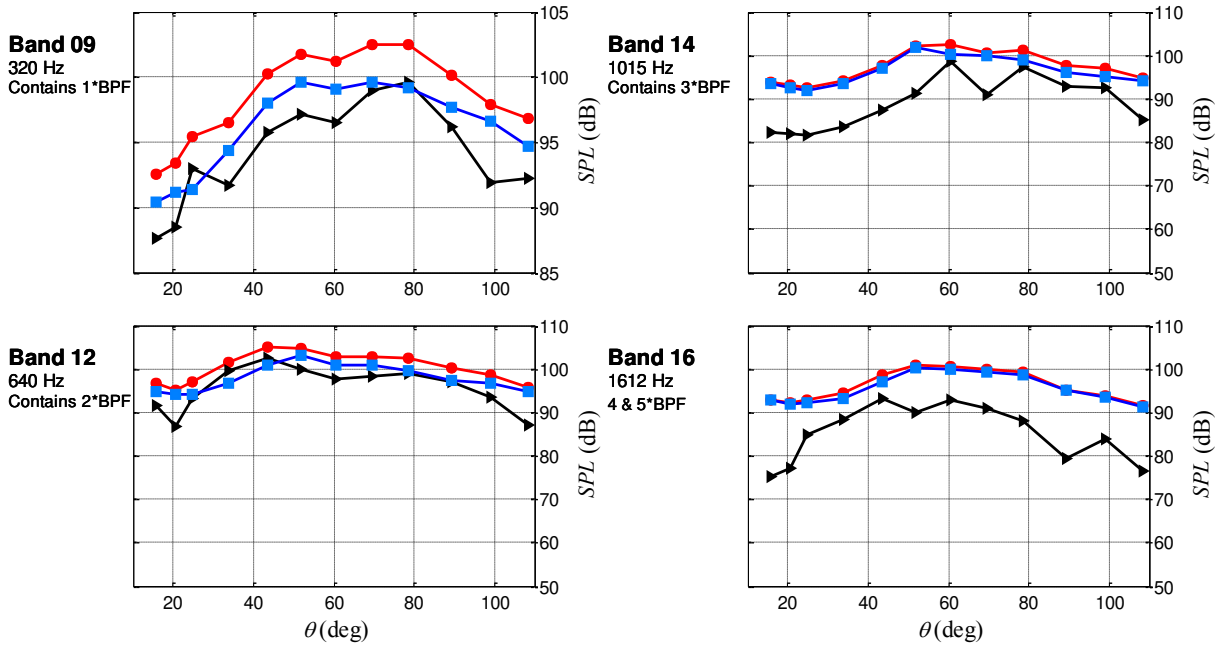


**Figure 13. One-third octave band directivities for four bands. Full-scale frequencies are shown. Total signal (red), broadband (blue), harmonic (black).**

### D. Overall Sound Pressure Level

Integrated noise metrics such as the overall sound pressure level (OASPL) describe the total energy contained in the spectrum. The OASPL was calculated by integrating the lossless SPL spectrum over all resolved frequencies. Fig. 14 plots the OASPL versus polar angle for the total, harmonic, and broadband signals. For the total and broadband component the energy peaks near $\theta = 60°$. The tonal component has a double peak at $\theta = 40°$ and 80°, an its level is at least 5 dB below the broadband level. The tonal component shows a sharp drop-off with polar angle away from the range of peak emission.

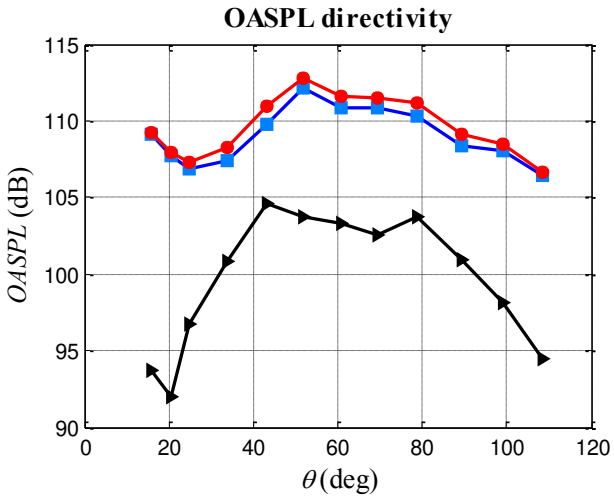


**Figure 14. OASPL directivity for the noise components. Total signal (red), broadband (blue), harmonic (black).**



## E. Comparison with NASA Large Scale Tests

In this section we make qualitative comparisons of our results with large-scale fan acoustic data acquired at NASA Langley's 9'× 15' tunnel using a continuously traversing microphone.[20,21] There are significant differences in the fan design and operating conditions between the UCI and NASA rigs. A quantitative comparison in thus impossible. However, the NASA experiment being the only known fan test where a signal decomposition was carried out, we are compelled to try a qualitative comparison.

**Table 3. Summary of fan specifications and experimental conditions**

| Quantity | UCI | NASA |
|---|---|---|
| Scale | 1:38 | 1:5 |
| Diameter | 2.67 in | 22 in |
| $M_{tunnel}$ | 0 | 0.1 |
| $M_{tip}$ | 0.61 | 1.08 |
| Rotor count | 14 | 22 |
| Stator count | 24 | 26 |
| FPR | 1.15 | 1.47 |
| Power | 6.7 hp | 5000 hp |
| Fan hub/ tip ratio | 0.42 | 0.30 |
| Scan Method | Fixed array | Continuous scan |
| Polar angle | 15° to 110° | 46° to 152° |

Table 3 summarizes the sizes, operating conditions, and measurement approaches of the two experiments. The most important operational difference was that the NASA rotor was transonic, while the UCI rotor was subsonic. Consequently, the NASA rotor emitted multiple pure tones (MPTs), in addition to the conventional tonal and broadband noise. MPTs are caused by the formation of leading-edge shocks on the suction side of the blades.[36] The resulting nonlinear quadrupole term transfers acoustical energy from BPF harmonics to other modes that radiate upstream.[37] For a perfect fan, with meticulous blade spacing and uniform blade geometry, the shock system will only emit energy at integer multiple of the BPF. However, natural manufacturing variations produce shocks of non-uniform amplitude and spacing, resulting in numerous tones in addition to the BPF harmonics. These additional harmonics are called MPTs and are often referred to as "buzz saw" noise. Some MPT harmonics can be louder than the BPF tones. Buzz saw tones are deterministic and are separated as a harmonic component.

From the measurement standpoint, the NASA tests utilized a single microphone traversing a straight sideline path at a speed of 0.0102 m/s (0.4 in/s), covering small to large polar angles $\theta$ (using UCI's geometric convention).[20] Because the microphone was moving continuously through the sound field the spatial resolution was practically infinite. In contrast, in the UCI experiment a number of stationary microphones were placed at fixed polar angles. Note that the range of polar angles was different in each experiment, UCI emphasizing the aft angles while NASA surveying mostly the forward angles. NASA's one-third octave spectra were interpolated to UCI's polar angles to facilitate comparisons. In addition, the UCI sound measurements were scaled to the distances along an axial traverse offset of 12 in. from the jet centerline.

Figure 15 compares the polar directivities of 1/3-octave bands of the UCI and NASA experiments, both scaled to the full-scale diameter of 2.67 m. The comparison is done at similar, although not identical, frequency bands. The first comparison band includes the 1×BPF harmonic, and the second comparison band includes 4 & 5×BPF (UCI) and 4×BPF (NASA). The NASA bands include MPTs, as discussed above. At low frequency, the harmonic content of the NASA fan is stronger than that of the UCI fan, possibly because of the presence of the MPTs. At higher frequency the broadband component dominates in both tests, the harmonic spectrum being on on the order of 10 dB below the broadband spectrum. It is significant that the small-scale test captures the high-frequency trends measured in the NASA facility.

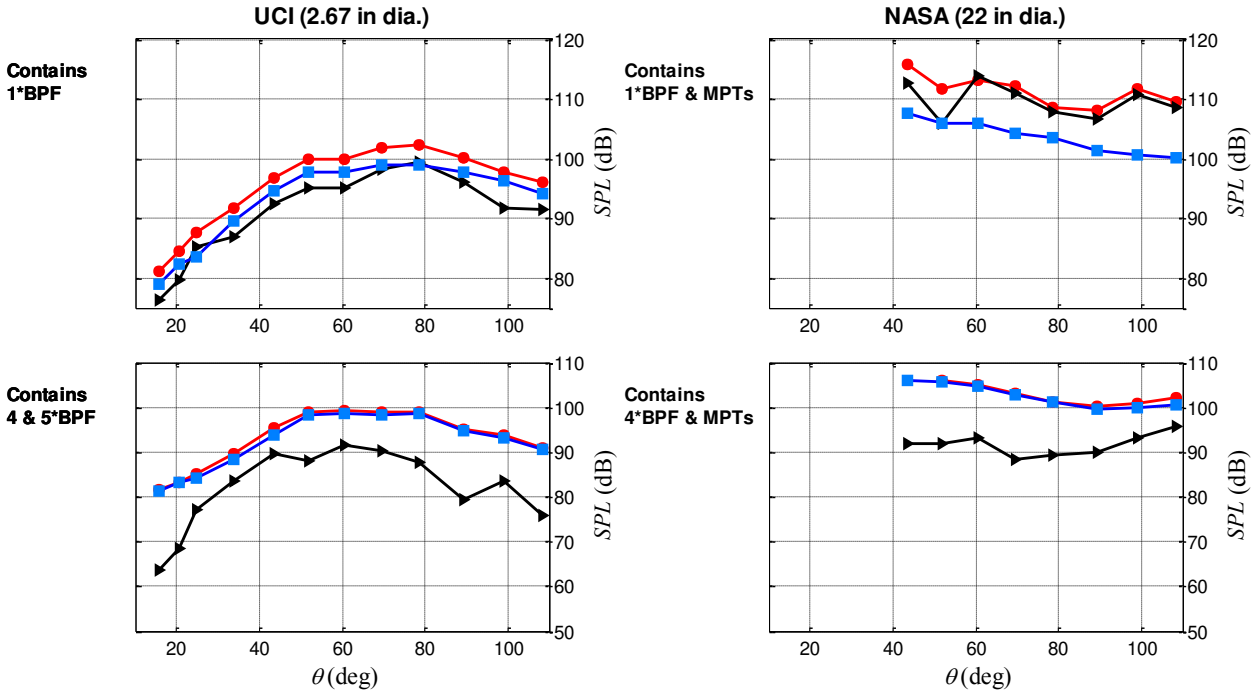


**Figure 15. Comparison of UCI and NASA one-third octave band directivities. Total signal (red), broadband (blue), harmonic (black).**

## V. Concluding Remarks

This project demonstrated the application of Vold-Kalman filtering of aeroacoustic measurements from a small scale ducted fan, for the purpose of rigorously determining the harmonic and broadband components of noise. Knowledge of the tonal and broadband noise content is essential for characterizing the fan noise source and predicting propulsion-airframe integration effects. The rapid-prototyped ducted fan featured a 14-bladed rotor and 24 stators, and operated at fan pressure ratio of 1.15 and rotor tip Mach number of 0.61. Its operation was representative of future geared turbofan engines with very large bypass ratio. A second-generation Vold-Kalman filter was employed to separate the time-domain contributions of harmonic and broadband contents. This filter is advantageous to frequency domain methods since it can easily localize information with high resolution needed to correct for the non-stationary behavior in real world experiments.

The results shows that the energies of the tonal and broadband contents are similar for the lower frequency bands, while the broadband component dominates the higher frequency bands. Corresponding trends in energy distribution between the components were found in large-scale NASA experiments. There are distinct differences in the polar directivities of the harmonic and broadband noise. The Vold-Kalman filter has proven effective and useful for separating the noise components. The ultimate importance of harmonic-versus broadband noise will be determined by the perceived noise level metric, which includes tone corrections. This was outside the scope of the present paper but will be the topic of future studies.

Complementing our earlier studies of the isolated and installed small-scale ducted fan,[16] this work demonstrates that important aspects of fan noise can be studied at low cost in university-scale facilities, leveraging advances in additive manufacturing and brushless motor technology. Innovative processing methods such as the Vold-Kalman filter can be applied not only to the signals of the individual microphones but also to time-series-based acoustic imaging. The combination of inexpensive test rigs with advanced measurement and processing methods (such as the continuous-scan technique used at NASA) holds promise for fundamental gains in our knowledge of the fan noise source and for constructing models for fan noise and its interactions with the airframe.



**Acknowledgment**

We thank Dr. Hävard Vold of ATA Engineering, Inc., for his advice and guidance on the formulation of the Vold Kalman filter for our experiment, and for enabling comparisons with his code.

## References

[1]Gerhold, C., Clark, L., and Dunn, M., "Investigation of Acoustic Shielding by Wedge-Shaped Airframe," *Journal of the Sound and Vibration*, Vol. 294, No. 1-2, 2006, pp. 49–63.

[2]Mayoral, S. and Papamoschou, D., "Effects of Source Redistribution on Jet Noise Shielding," AIAA 2010-0652, Jan. 2010.

[3]Thomas, R. and Burley, C., "Hybrid Wing Body Aircraft System Noise Assesment with Propulsion Airframe Aeroacoustic Experiments," AIAA 2010-3913, 2010.

[4]Berton, J., "Empennage Noise Shielding Benefits for an Open Rotor Transport," AIAA 2011-2764, June 2011.

[5]Truong, A. and Papamoschou, D., "Aeroacoustic Testing of Open Rotors at Very Small Scale," AIAA 2013-0217, Jan. 2013.

[6]Liebeck, R., "Design of the Blended Wing Body Subsonic Transport," *Journal of Aircraft*, Vol. 41, No. 1, 2004, pp. 10–25.

[7]Magliozzi, B., Hanson, D., and Amiet, R., "Propeller and Profan Noise," Tech. Rep. N92-10598 01-71, NASA Langley Research Center, Hampton, VA, July 1991.

[8]Topol, A., Ingram, C., Larkin, M., Roche, C., and Thulin, R., "Advanced Subsonic Technonolgy (AST) 22-Inch Low Noise Research Fan Rig Preliminary Design of ADP-Type Fan 3," Tech. Rep. NASA/CR-2004-212718, NASA Langley Research Center, Hampton, VA, Feb 2004.

[9]Hughes, C., Jeracki, R., Woodward, R., and Miller, C., "Fan Noise Source Diagnoistic Test-Rotor Alone Aerodynamics Performance Results," NASA/TM-2005-211681 (AIAA-2002-2426), April 2005.

[10]Heidelberg, L., "Fan Noise Source Diagnostic Test - Tone Model Structure Results," NASA/TM-2002-211594 (AIAA-2002-2428), April 2002.

[11]Morin, B., "Broadband Fan Noise Prediction System for Turbofan Engines, Volume 1: Setup BFANS User's Manual and Developer's Guide," Tech. Rep. CR-2010-216898, NASA, Nov 2010.

[12]Morin, B., "Broadband Fan Noise Prediction System for Turbofan Engines, Volume 3: Validation and Test Cases," Tech. Rep. CR-2010-216898, NASA, Nov 2010.

[13]Hughes, C., Jeracki, R., Woodward, R., and Miller, C., "Aerodynamic Performance of Scale-Model Turbofan Outlet Guide Vanes Designed for Low Noise," NASA/TM-2001-211352 (AIAA-2002-0374), Dec. 2001.

[14]Woodward, R., "Comparison of Far-Field Noise for Three Significantly Different Model Turbofans," *AIAA Paper 2008-0049*, Jan 2008.

[15]Woodward, R., Elliott, D., Higher, C., and Berton, J., "Benefits of Swept-and-Leaned Stators for Fan Noise Reduction," *AIAA Journal*, Vol. 38, No. 6, 2001.

[16]Truong, A. and Papamoschou, D., "Experimental Simulation of Ducted Fan Acoustics at Very Small Scale," AIAA 2014-0718, Jan. 2014.

[17]Parry, A.B., K. M. and Tester, B., "Relative importance of open rotor tone and broadband noise sources," AIAA 2011-2763, June 2011.

[18]Stephens, D. and Envia, E., "Acoustic Shielding for a Model Scale Counter-Rotation Open Rotor," NASA/TM-2012-217227 (AIAA-2011-2940), Jan. 2012.

[19]Sree, D. and Stephens, D., "Tone and Broadband Noise Separation from Acoustic Data of a Scale-Model Counter-Rotating Open Rotor," AIAA 2014-2744, June 2014.

[20]Shah, P., Vold, H., Hensley, D., E., E., and D., S., "A High-Resolution, Continuous-Scan Acoustic Measurement Method for Turbofan Engine Applications," ASME Paper GT2014-27108, June 2014.

[21]Stephens, D. and Vold, H., "Order Tracking Signal Processing for Open Rotor Acoustics," *Journal of Sound and Vibration*, Vol. 333, No. 16, 2014, pp. 3818–830.

[22]Fyfe, K. and Munck, D., "Analysis of Computed Order Tracking," *Mechanical Systems and Signal Processing*, Vol. 11, No. 2, 1997, pp. 187–205.

[23]Vold, H. and Leuridan, J., "High Resolution Order Tracking at Extreme Slew Rates Using Kalman Tracking Filters," SAE Technical Paper 931288, May 1993.

[24]Tuma, J., "Setting the Passband Width in the Vold-Kalman Tracking Filter," 12th International Congress on Sound and Vibration, 2005.

[25]Feldbauer, C. and Holdrich, R., "Realization of a Vold-Kalman Tracking Filter- A Least Squares Problem," Proceedings of the COST-6 Conference on Digital Audio Effects (DAFX-00), Dec. 2000.

[26]Kalman, R., "A New Approach to Linear Filtering and Prediction Problems," *Journal of Basic Engineering, Transactions of ASME*, Vol. 82, 1960, pp. 35–45.

[27]Herlufsen, H., Gade, S., Hansen, K., and Vold, H., "Characteristics of the Vold-Kalman Order Tracking Filter," Bruel and Kjaer Technical Review, April 1999.

[28]Wold, H., *A Study in the Analysis of Stationary Time Series*, Ph.D. thesis, Stockhom University, 1938.

[29]Huang, N., Wu, M., Qu, W., Long, S., and Shen, S., "Applications of Hilbert-Huang transform to non-stationary financial time series analysis," May 2009, pp. 245–268.

[30]Cohen, M., *Analyzing Neural Time Series Data*, The MIT Press, Cambridge.

[31]Oweis, R. and Abdulhay, E., "Seizure Classification in EEG Signals Utilizing Hilbert-Huang Trasnform," *Biomedical Engineering Online*, May 2011, pp. 10–38.

[32]Feldman, M., "Hilbert Transform In Vibration Analysis," *Mechanical Systems and Signal Processing*, Vol. 25, No. 3, April 2011, pp. 735–802.

[33]Cohen, L. and Lee, C., "Standard Deviation Of Instantaneous Frequency," *Acoustic, Speech, and Signal Processing*, Vol. 4, 1989, pp. 2238–2241.

[34]Kovacic, I. and Brennan, M., *The Duffing Equation: Nonlinear Oscillators and their Behavior*, John Wiley and Sons, New Jersey, 1st ed., 2011.

[35]Vold, H., "Sine Waves Are Stubborn Things," Sound and Vibrations, June 2013.

[36]Goldstein, A., Glaser, F., and Coats, J., "Acoustic Properties of a Supersonic Fan," NASA/TN-1973-15025, Jan. 1973.

[37]Han, F., Shieh, C., Sharma, A., and Paliath, U., "Multiple Pure Tone Noise Prediction and Comparison with Static Engine Test Measurement," AIAA 2007-3523, May 2007.